Characteristics of defect modes in side-coupled and mutually coupled microresonator arrays

Tobing, Landobasa Yosef Mario A. L.; Tjahjana, Liliana; Zhang, Dao Hua

2012

Tobing, L. Y. M. A. L., Tjahjana, L., & Zhang, D. H. (2012). Characteristics of defect modes in side-coupled and mutually coupled microresonator arrays. Journal of the optical society of America B : optical physics, 29(4), 738-747.

https://hdl.handle.net/10356/79989

https://doi.org/10.1364/JOSAB.29.000738

Characteristics of defect modes in side-coupled and mutually coupled microresonator arrays

Landobasa Y. M. Tobing,[1,2] Liliana Tjahjana,[1] and Dao Hua Zhang[1,3]

[1]*Nanophotonics Laboratory, S1-B2A-02, 50 Nanyang Avenue, Nanyang Technological University, Singapore 639798, Singapore*
[2]*e-mail: ltobing@pmail.ntu.edu.sg*
[3]*e-mail: edhzhang@ntu.edu.sg*

Received November 22, 2011; revised January 24, 2012; accepted January 24, 2012; posted January 24, 2012 (Doc. ID 158406); published March 21, 2012

We present both theoretically and experimentally the existence of defect modes in side-coupled and mutually coupled microresonator arrays. The qualitative difference between the two types of defect modes is investigated. The Q factor of both defect modes for varying defect sizes is characterized, and an enhancement of ~30× relative to individual loaded resonators is demonstrated. The defect modes are then compared with coupled resonator–induced transparency (CRIT), indicating that the defect modes based on side-coupled microresonator arrays are actually the extension of the CRIT resonance in two-resonator structures.

OCIS codes: 130.3120, 230.4555.

1. INTRODUCTION

The study of coupled optical resonators has gained much attention because of its ability to provide an optical analog of existing mechanisms in atomic systems without the need to sustain their coherent properties in low temperature [1]. A notable example is in the optical mimicking of electromagnetically induced transparency (EIT) [2] based on a two-resonator system, which results in the generation of ultrahigh Q resonance that can potentially be used for light-storing applications [3,4]. However, the generation of high Q resonance using coupled resonators is not always based on an EIT-like mechanism [5–9] but also is based on different interactions between two resonators [10,11], between direct and indirect resonant pathways [12,13], and on many resonator systems.

In a periodic array of optical resonators [14–17], the analog can be extended in that the interaction between the resonators mimics the interaction between bound electrons in a semiconductor, which in turn results in the formation of continuous photonic bands with certain dispersion characteristics. Indeed, such a combination of photonic crystal and resonator properties has enabled the coupled resonator configuration to be an interesting structure for slow-light applications [16,18,19], high order filters [20–23], and nonlinear frequency conversion [24]. Generally, there are two configurations by which resonators can be periodically arranged. In the first type (Type I), the resonators are evenly spaced with each other and side coupled with two common optical waveguide buses. This is commonly known as the side-coupled integrated spaced sequence of resonator (SCISSOR) [14]. In the second type (Type II), identical resonators are mutually coupled to one another, with the first and the last resonators directly coupled to input and output waveguide buses. This structure is commonly known as the coupled resonator optical waveguide (CROW) [16]. Recently, the concept of CROW has been extended to an array of alternating resonators, where each unit cell consists of two dissimilar resonators. It has been theoretically shown that using the diatomic coupled resonator waveguide [25], the drop port passband, and the delay spectra can be engineered through small changes in the interresonator coupling or waveguide refractive indices.

The mutual coupling between resonators in Type II is functionally identical to semitransparent mirrors, which makes it analogous to an array of mirror stacks, where each mirror represents the interface between adjacent resonators. Likewise, for the Type I structure, the add-drop process in each resonator is analogous to the frequency dependent mirror, which makes it functionally resembling distributed feedback structures, such as those in Bragg gratings. Thus, the interresonator interactions, which are inherent in either Type I or Type II structures, can be combined in a synergistic manner so as to generate desired spectral characteristics. Examples can be found when resonators with embedded discontinuity are periodically side coupled with a single bus waveguide [26], or when resonators are side coupled with a single bus waveguide embedded with an array of reflectors [27].

Similar to their conventional photonic crystal case [28], defect modes can be excited when irregularities are introduced into an otherwise periodic array of resonators [29,30], which translates to high Q resonance corresponding to strong light localization within such a defect. In a coupled resonator array structure, the defects are introduced in the way described in Fig. 1. For the Type I structure, the defect may be introduced in the form of dislocation, where the interresonator distance at the center of the array is longer (or shorter). For the Type II structure, the defect is introduced when the resonator at the center of the array has a different size compared to the rest. The defect is "donorlike" ("acceptorlike") when the defect is larger (smaller) than the size of the regular unit cell, which can be the interresonator spacing (for Type I) or cavity length (for Type II). Alternatively, active means can also be used to introduce defects in resonator arrays, where positive (negative) refractive index perturbation gives rise to donorlike

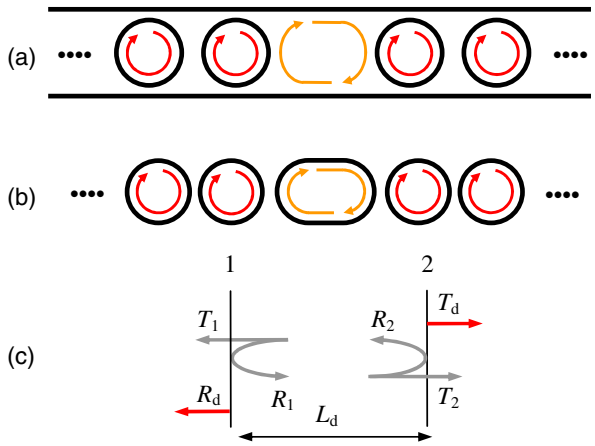

Fig. 1. (Color online) A single (point) defect embedded in a (a) SCISSOR (Type I), and (b) CROW (Type II). (c) The Fabry–Perot cavity formed by the defect and the two subarrays.

(acceptorlike) defects. The extensive treatment of defect modes in coupled resonator configurations for both types has been theoretically investigated in our previous work [29]. Thus far, the existence of defect modes based on the coupled resonator structure has been experimentally demonstrated for the Type II structure [31], but not for the Type I structure.

To a certain degree, it can be said that the Type I defect mode structure presented in this paper is a topological extension of the two-resonator system for the EIT-like resonance [5]. Such a topological extension also suggests that the field distributions of the two seemingly different mechanisms are related. The EIT-like resonance is the result of coherent interaction between two decaying optical fields originated from the two resonators along the two side waveguides [5]. On the other hand, the high-Q resonance in the Type I defect mode is the result of light localization within the photonic bandgap region. In this paper, we experimentally characterize the defect modes based on indirectly coupled (Type I) and mutually coupled (Type II) resonator arrays, and explore the transition from EIT-like resonance in the two-resonator system toward the defect modes in the coupled resonator array.

2. CHARACTERISTICS OF DEFECT MODES IN TYPE I AND TYPE II STRUCTURES

As shown in Fig. 1(c), any defect mode configurations can be represented as a defect layer of thickness L_d sandwiched by two subarrays functioning as frequency dependent mirrors, where $R_{1,2}$ and $T_{1,2}$ are the reflection and transmission coefficients of the respective subarrays. The definition of L_d depends on the defect mode configurations. For the Type I structure, L_d is the interresonator spacing of the defect, while for the Type II structure, L_d is half of the cavity length of the defect resonator. The system transmission coefficient (T_d) is found by totaling the transmitted waves:

$$T_d = T_1T_2\ \exp(-i\delta_d/2)\sum[R_1R_2\exp(-i\delta_d)]^m = \frac{T_1T_2\ \exp(-i\delta_d/2)}{1-R_1R_2\ \exp(-i\delta_d)}, \quad (1)$$

where $\delta_d = 2k_0n_{\text{eff}}L_d$ is the phase change accumulated in a defect. The defect transmission is on-resonance when $\phi_{R1} + \phi_{R2} - \delta_d = m2\pi$ is satisfied, where m is the mode number. This condition then determines the frequencies of the defect mode. Normally the defect mode exists for $m = 0$, for which the defect modes for a symmetric structure ($R_1 = R_2 = R$) follow the condition

$$2\phi_R = \delta_d, \quad (2)$$

where φ_R is the phase response of reflection from any type of finite subarrays (Type I or Type II). In the case of infinite subarrays, the reflection of both types can be expressed by the Bloch theorem [29]

$$R_{\text{I}} = -\frac{m_{12}}{m_{11}-\exp(ik\Lambda)}, \qquad R_{\text{II}} = -\frac{p_{12}}{p_{11}-\exp(ik\Lambda)}. \quad (3)$$

Here, k is the Bloch wave vector, Λ is the structure periodicity, and $[m]$, $[p]$ are the transfer matrix expressions for one unit cell of Type I and Type II, respectively. The transfer matrix formalism for both types has been investigated in our previous work [17], and the detailed expression of $[m]$ and $[p]$ are given in the Appendix.

Equation 2 is solved for the Type I configuration, and the associated defect resonance frequency is mapped as a function of the normalized defect size ($=L_d/L_{\text{cav}}$) in Fig. 2(a). The cavity length is defined as the circumference of the resonator, i.e., $L_{\text{cav}} = (2\pi R + 2L_C)$, where L_C is the coupler length. The interresonator spacing in the subarrays is fixed to half of the cavity length, i.e., $\Lambda = 0.5L_{\text{cav}}$, while the defect size is varied from $0.5L_{\text{cav}}$ ($L_d = \Lambda$) to $0.6L_{\text{cav}}$ ($L_d = 1.2\Lambda$). The traces of donorlike modes can be observed as the defect size is increased ($L_d > \Lambda$), where the modes move in the direction from the upper continuous band (photonic conduction band) to the lower continuous band (photonic valence band). In general, there are two donorlike modes in the Type I structure. One donor mode starts to emerge from the photonic conduction band whenever the other mode reaches the center of the photonic bandgap.

The defect transmission corresponding to $L_d = 0.52L_{\text{cav}}$ ($L_d = 1.04\Lambda$) is calculated using transfer matrix formalism and is shown in Fig. 2(b), where each subarray has $N = 5$ resonators. In this case, the coupling coefficient between each resonator and bus waveguide is chosen to be $r = 0.85$. Indeed, the locations of defect resonance from finite case transfer matrix formalism are in good agreement with those calculated from defect mode mapping based on Bloch modes. In general, the Q factor increases when the defect mode is approaching the midgap. This is to be expected since the subarray reflectivity is at maximum when the rings are on resonance (or at the midgap). It should be noted that the trace is not continuous at $L_d = 0.5L_{\text{cav}}$, suggesting the nonexistence of defect modes. This is to be expected since at $L_d = 0.5L_{\text{cav}}$ the Type I structure appears exactly as a SCISSOR structure, which has $2N + 1$ identical resonators. Thus, a defect mode cannot exist by definition. Alternatively, from the perspective of defect mode mapping, $L_d = 0.5L_{\text{cav}}$ corresponds to a situation where the subarray reflectivity reaches unity, which then leads to infinite Q resonance, at least in the lossless case. In the presence of slight cavity loss, such resonance is suppressed entirely.

The mapping of the Type II defect mode is shown in Fig. 3(a), where the defect resonator size is increased from $1.0L_{\text{cav}}$ to $1.2L_{\text{cav}}$. The trace of donorlike modes can be observed, as expected. However, it should be noted that

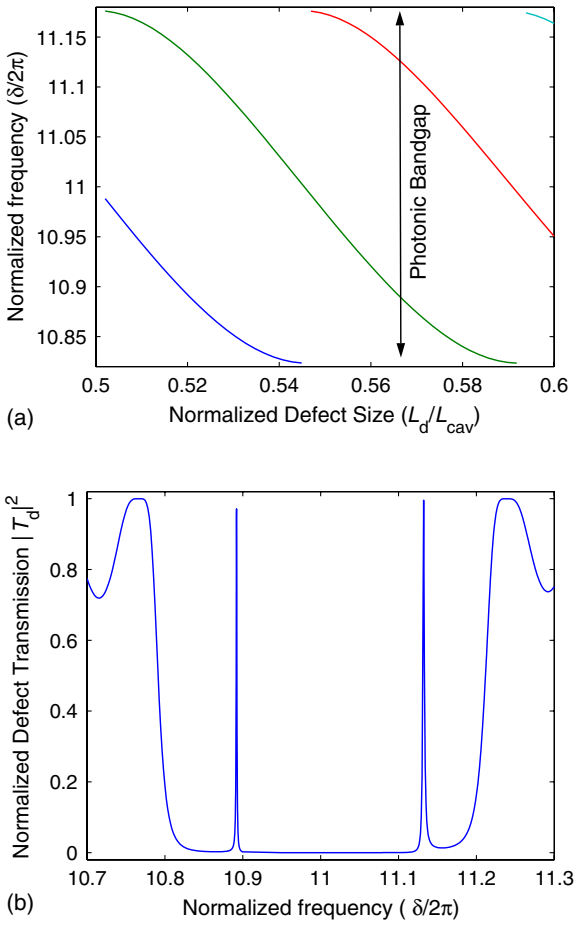

Fig. 2. (Color online) (a) Frequencies of the defect modes versus the defect length for infinite Type I periodic structure. (b) Defect transmission $|T_d|^2$ for $N = 5$, when $L_d = 0.52L_{cav}$. The coupling coefficient and the mode number are $r = 0.85$ and $m = 10$, respectively.

another donor mode starts to emerge only after the existing donor mode makes a complete path from the upper to the lower conduction band. This means that there is only one excited donor mode in the Type II structure, in contrast with the case of the Type I structure, which has two excited donor modes. This is attributed mainly to the nature of coupling between the subarrays and the defect. In Type I the defect interacts with the subarrays when the rings are on resonance, which means the round-trip phase of the defect is significantly perturbed by the resonant process of the subarrays. In addition, reflection between the two subarrays readily imparts a 2π phase jump, as evident from Eq. (2). This is equivalent to one resonance order, and it is sufficient to excite another defect mode in the Type I structure. On the other hand, in the Type II structure the defect interacts with subarrays when the rings are off resonance where the phase is relatively frequency independent. Thus, the resonance condition of the defect in the Type II structure is determined only by the defect.

The relationship of the Q factor to the defect resonance location is the same as that in Type I. However, in contrast to the Type I defect mode, the Q factor of the Type II defect mode does not go to infinity at the midgap. This is because the subarray reflectivity is always lower than unity in the finite-sized subarrays, which is a consequence of the formation of the photonic bandgap around the antiresonance of the resonators. The photonic bandgap is better defined when more unit cells are introduced into the subarrays, and the subarrays reflectivity approaches unity when the subarray is semi-infinite in size. In the Type I structure, on the other hand, the subarray reflectivity is by nature resonance assisted, which by virtue of constructive interference may give unity reflection even in finite size subarrays. Figure 3(b) shows the transmission of Type II defect modes when the defect length is $L_d = 1.05L_{cav}$ and the subarray consists of $N = 3$ resonators with the interresonator coupling coefficient of $r = 0.65$.

Analogous to the Fabry–Perot etalon, by using Eq. (1) the resonance linewidth for a defect mode can approximately be given by $\Delta\delta_{FWHM} = 2(1 - R_1^2)/R_1$. Indeed, this shows the dependence of the Q factor on subarray reflectivity, which is a function of subarray size, defect mode detuning relative to the midgap, and coupling coefficients. A closer detuning toward the midgap and the introduction of more unit cells within the subarrays increase the subarray reflectivity and hence lead to a higher Q factor. Alternatively, the Q factor can be increased when the coupling strength is increased (decreased) in Type I (Type II) structures. The field distribution of the defect mode in both types is [29] $A_d(n) = x_0 \exp(-nk\Lambda)$, where n signifies the nth unit cell from the defect and x_0 is the field amplitude of the defect. Note that the Bloch wave vector k is imaginary within the photonic band-

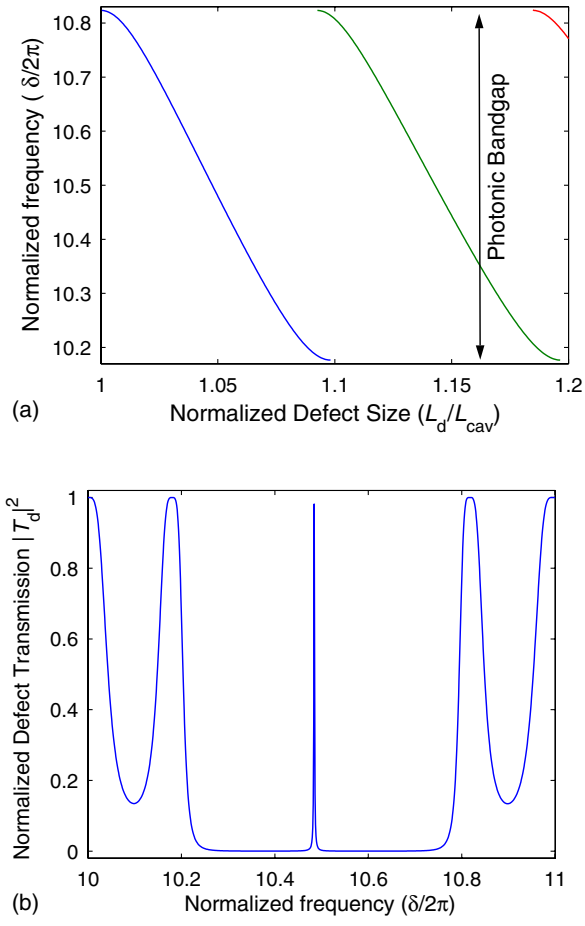

Fig. 3. (Color online) (a) The resonant frequency of defect modes versus normalized defect length L_d/L_{cav}. (b) Defect transmission $|T_d|^2$ for $N = 3$. The defect is a racetrack resonator whose cavity length is $L_d = 1.05L_{cav}$. The coupling coefficient and the mode number is $r = 0.65$ and $m = 10$, respectively.

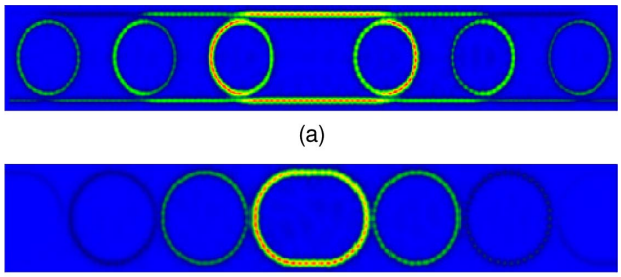

Fig. 4. (Color online) Absolute amplitude of the field distribution calculated by FDTD for (a) Type I ($L_d/L_{\mathrm{cav}} = 0.75$) and (b) Type II ($L_d/L_{\mathrm{cav}} = 1.1$).

gap, which means that the field decays as a function of n, indicating a constant amplitude (in the lossless system) within one unit cell.

In numerical simulation, the field distribution corresponding to the defect mode in coupled resonator arrays with arbitrarily large subarrays cannot be obtained by normal external excitation. This is because the light cannot penetrate into the defect because of the strong reflection from the subarrays. Thus, this limits the maximum obtainable Q factor in numerical simulation. In the Type I structure, for example, the reflection occurs by means of Bragg reflection, which comes from constructive interference of decaying optical fields from each resonator. The coupling strength between the resonator and the waveguide bus therefore should be made fairly small to make the incoming light penetrate the defect. In the Type II structure, on the other hand, the light is strongly reflected near the antiresonance. So the coupling strength should be fairly strong to penetrate the defect ring. The external excitation, however, is sufficient for obtaining the defect transmission spectrum.

Hence, the defect mode field distribution can be obtained only by internal excitation of the defect. In the finite difference time domain (FDTD) simulations, a Gaussian input pulse is launched from the waveguide near the dislocation (for Type I) or defect ring (for Type II), and the intracavity power is monitored as a reference. The defect mode corresponds to sharp and high contrast transmission within the photonic bandgap region. The field distribution corresponding to such a defect mode is obtained by iterative adjustment of the Gaussian pulse input frequency until convergence is met. Figure 4 shows the field distributions corresponding to Type I and Type II defects, which show good agreement with those calculated by the Bloch theorem. In the Type I structure shown in Fig. 4(a), the field amplitudes along the bus waveguides are piecewise constant between two resonators. This agrees with the fact that the eigenvector at a given Bloch wave vector is defined as the set of field amplitudes along the waveguides. The same agreement is found in the Type II structure shown in Fig. 4(b), where the optical field amplitude is constant within each resonator but decays in the direction away from the defect ring.

3. EXPERIMENTS

The experimental demonstration of our defect modes is carried out in silicon-on-insulator (SOI) technology using complementary metal oxide semiconductor (CMOS)–compatible 193 nm deep UV lithography [32]. The silicon waveguide core is 450 nm wide and 220 nm thick, while the buried oxide is 2 μm thick. The upper cladding is SiO_2 deposited by plasma enhanced chemical vapor deposition (PECVD) at 300 °C for 600 nm nominal thickness. The input and output interface is facilitated by second order gratings, which are integrated at both ends of the devices. The grating is of 70 nm etch depth and 630 nm grating pitch. In this fabrication batch, the gratings are made to be curved in shape so that the light is coupled and focused simultaneously onto the submicron SOI waveguide. Using this method, more compact grating couplers can be realized with about the same grating efficiency and lower mode-conversion loss, which thus increases the device density on the chip. The tunable laser used in this work is Santec TLS-510 (1510 nm$\leq\lambda\leq$ 1630 nm, and $\Delta\lambda < 1$ pm), while the light detector is the fiber-based ILX FPM-8210.

In addition to the Type I and Type II defect mode structures to be demonstrated in this paper, various basic structures such as straight waveguides and racetrack ring resonators were also fabricated in the same sample. Measurement of straight waveguides of different lengths shows a waveguide propagation loss of $\alpha \sim 2.84$ dB/cm (for SiO_2 cladding) and grating coupling loss of ~5 dB/grating. In the design, the ring cavity is optically excited by means of evanescent coupling from the waveguide, where the gap separation between the ring and the waveguide is 200 nm. The ring radius in all our devices is fixed to 5 μm. As the coupling coefficient is dependent on both gap separation and coupler length, the racetrack geometry is employed in our resonator structures for the purpose of obtaining easier control of coupling coefficients. Ring resonators of racetrack geometry for different coupler lengths are then characterized to obtain group index (n_g), cavity round-trip loss (a), and coupling coefficients (r). From the cavity spectral range the group index is measured to be $n_g \sim 4.25$. The cavity round-trip loss and coupling coefficients are obtained from curve fitting of the drop spectra. The cavity loss is found to be $a \sim 0.994$ [33], and the coupling coefficient as a function of coupler length (L_C) can be empirically written as

$$r = \cos[\pi L_C/(2L_\pi) + \phi_0] \tag{4}$$

with L_π as the beating length of the coupler and φ_0 as the lumped phase indicating the contribution of the curved waveguide in the racetrack resonator. The deduced L_π and φ_0, for 200 nm gap and 5 μm ring radius, are 23.29 μm and 0.1957 rad, respectively.

Figure 5 shows the coupling coefficients and loaded Q factor as a function of coupler length, where the experimentally deduced L_π and φ_0 are used to calculate the coupling coefficients for arbitrary coupler lengths. The micrograph of the racetrack ring resonator and coupler are shown in the insets of Fig. 5. The cavity finesse ($F = \Delta\lambda_{\mathrm{FSR}}/\Delta\lambda$) for a given coupling coefficients (r) and cavity loss (a) is calculated by

$$F = \frac{\pi\sqrt{ar^2}}{1 - ar^2}, \tag{5}$$

which translates to the Q factor when multiplied by resonance mode number ($m = \lambda/\Delta\lambda_{\mathrm{FSR}} = n_g L_{\mathrm{cav}}/\lambda$)

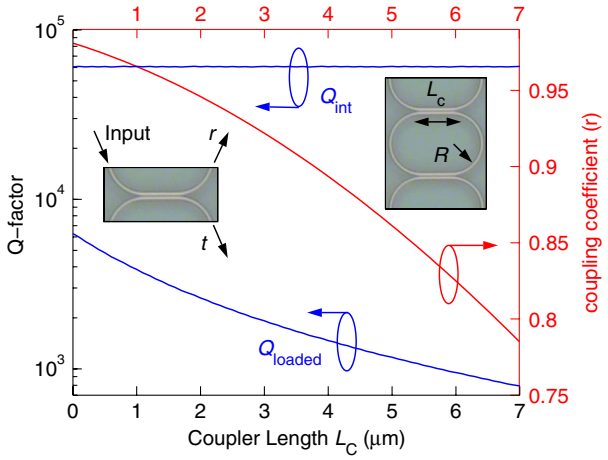

Fig. 5. (Color online) Relationship between coupler length (L_C), coupling coefficient (r), and Q factor (Q). The cavity loss is assumed to be $a \sim 0.994$. The directional coupler and the racetrack ring resonator are shown in the insets.

$$Q \equiv \frac{\lambda}{\Delta\lambda} = \left(\frac{\lambda}{\Delta\lambda_{\mathrm{FSR}}}\right)\left(\frac{\Delta\lambda_{\mathrm{FSR}}}{\Delta\lambda}\right) = mF. \tag{6}$$

Likewise the intrinsic Q factor Q_{int} is calculated by $Q_{\mathrm{int}} = mF_{\mathrm{int}}$, where F_{int} is the cavity finesse for unloaded resonator ($r = 1$),

$$F_{\mathrm{int}} = \frac{\pi\sqrt{a}}{1-a}. \tag{7}$$

The deduction of cavity round-trip loss determines the maximum limit of the measurable Q factor in our defect mode devices. The loaded Q factor of a resonance is always limited to half of its intrinsic Q factor, $Q = Q_{\mathrm{int}}/2$. This corresponds to a familiar critical coupling situation [34] and maximum intracavity intensity buildup. Note that the cavity loss deduced from the racetrack resonator ($a \sim 0.994$) is larger than that deduced from the propagation loss of straight waveguide ($a \sim 0.998$). This is because of the mode-conversion loss within the racetrack resonator, which is associated with the mode overlap and index mismatch between the mode in the curved section and that in the straight section [35,36]. Although the mode-conversion loss can be avoided in point-coupling geometry, the coupling strength is generally small and makes the external excitation of defect modes difficult. Thus, racetrack geometry is used in our experiments to have stronger coupling strength at the expense of higher cavity loss. As denoted by the flat line in Fig. 5, the intrinsic Q factor is empirically calculated to be $Q_{\mathrm{int}} \sim 6 \times 10^4$. This is lower than the typical value of $Q_{\mathrm{int}} \sim 2 \times 10^5$ in the point-coupled ring resonator, which is rather expected because of the inherent mode-conversion loss in the racetrack geometry.

A. Type I Defect Modes

The fabricated Type I defect mode structure consists of identical racetrack resonators periodically side coupled with two common optical waveguides, with an elongated section at the center (see Fig. 6). In SCISSOR, the photonic bandgap is formed by two overlapping bandgaps originated from resonators and the Bragg mechanism [14,17]. The resonator bandgap is the strong reflection originated from the resonance property of an individual resonator, where the light is resonantly tunneled from one waveguide to another. The Bragg gap, on the other hand, arises from the constructive interference between decaying optical fields from each resonator. The Bragg resonance, just as in other Bragg structures, is satisfied when the periodicity Λ is an integer multiple of half wavelength, $n_{\mathrm{eff}}\Lambda = m(\lambda/2)$. These two bandgaps overlap when Λ is exactly a multiple of half-cavity length ($\Lambda = \mathrm{mL}_{\mathrm{cav}}/2$), and this results in a broader reflection band. Indeed, this is one of the salient features of the hybrid resonator photonic crystal structure, for which photonic bandgap can be realized in a fewer number of unit cells.

In the Type I defect mode structure, it is important to overlap the resonator and the Bragg gaps. A slight nonoverlapping of these bandgaps results in a very narrow spike, which has been termed a coupled resonator–induced transparency (CRIT) by another research group [37]. However, despite the existence of narrow transparency in the slightly nonoverlapped bands, it should be noted that the location of such transparency cannot be passively tuned and the Q factor mainly depends on the degree of nonoverlapping between the bands. More band nonoverlapping introduces a wider band in the transparency and may also give split peaks. Such splitting is, in fact, the inherent sidelobes of the Bragg mechanism, which comes from interresonator interference.

To ensure overlapping between Bragg and resonator gaps, curved optical channels are introduced into the Type I structure, as shown in Fig. 6. In each unit cell the waveguide forms an S bend (of $\pi/4$ arc) with bending radius exactly the same as the ring radius. Thus, the interresonator spacing is always equal to half of the cavity length for any coupler length. The other reason for using a curved waveguide in this work is to reduce loss related to mode mismatch in the evanescent coupling. Figure 7 shows the transmission spectrum of the Type I defect mode for different normalized defect sizes, which is defined by $k_d = L_d/L_{\mathrm{cav}}$. Here, each of the subarrays has four unit cells. The photonic bandgap corresponds to very low

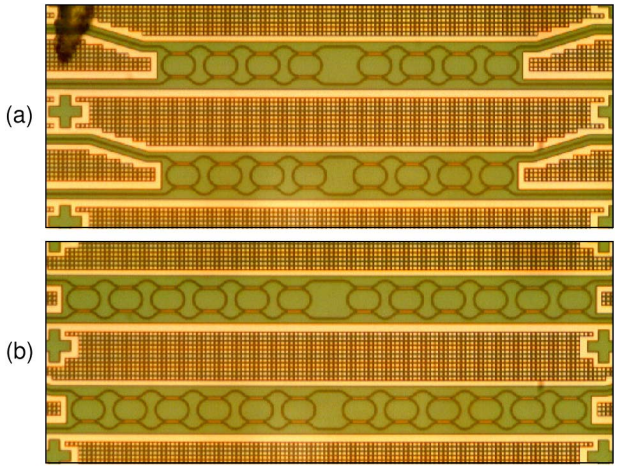

Fig. 6. (Color online) Optical micrograph of fabricated Type I defect mode structures. The subarrays are designed to have (a) four and (b) six unit cells. The defect is introduced by making the interresonator length longer than the regular ones. The optical waveguide is designed to be curved to prevent length mismatch between the interresonator spacing and the cavity length.

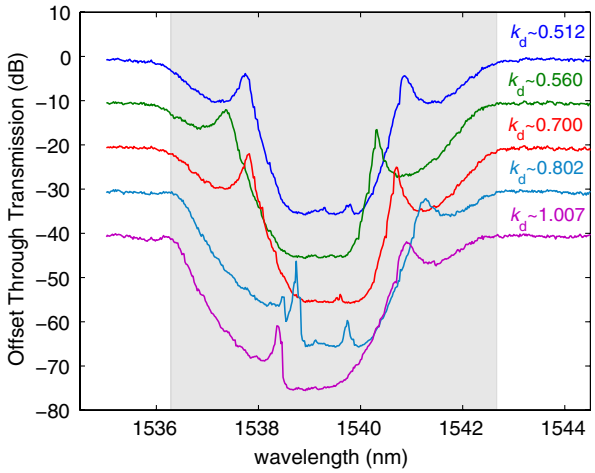

Fig. 7. (Color online) Offset dB through transmission of Type I defect modes for different normalized defect sizes (k_d). The subarray cell number is $N = 4$. The photonic bandgap is indicated by shaded region.

transmission and is indicated by the shaded region in the spectrum. The coupler length is designed to be $L_c = 5$ μm, which gives a coupling coefficient of $r \sim 0.86$ and a resonator loaded Q factor of $\sim 10^3$ (see Fig. 5). The defect lengths are 0.5 μm, 2.5 μm, 8.3 μm, 12.5 μm, and 21 μm, which correspond to normalized defect sizes of 0.512, 0.56, 0.7, 0.802, and 1.007, respectively.

At $k_d \sim 0.512$, we can see that the transmission spectrum is almost similar to that of SCISSOR ($k_d = 0.5$). When k_d is about 0.5, there are three defect modes, of which two peaks are situated near the band edge and the other is near the midgap. The two defect modes are clearly seen in the spectrum but not for the third one. This is because of the very high-Q factor associated with unity reflection from the subarrays, which is entirely suppressed by the presence of loss. For other defect lengths, defect modes at various locations within the photonic bandgap can clearly be observed, with increasing Q factor (becoming progressively symmetrical in line shape) in defect modes closer to the midgap. The plot of the Q factor of the defect modes as a function of normalized detuning from the midgap is shown in Fig. 8.

The Q factors are obtained from directly measuring the defect mode wavelength and its corresponding 3 dB linewidth

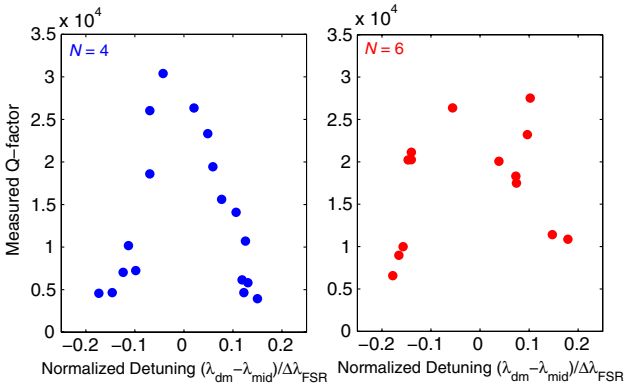

Fig. 8. (Color online) Q factor versus normalized detuning relative to midgap wavelength for $N = 4$ (left) and $N = 6$ (right). The case of $N = 6$ shows a less sensitive Q factor with respect to normalized detuning; however, it comes at the expense of more enhanced loss.

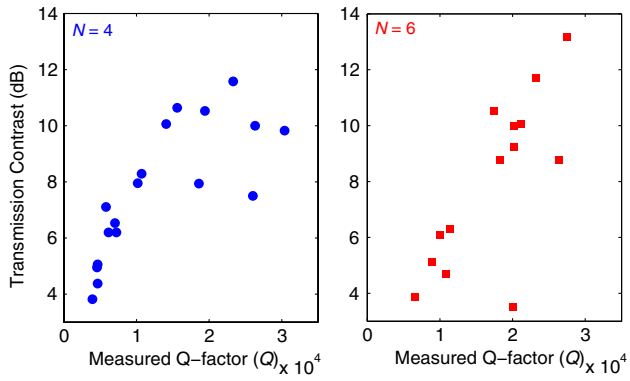

Fig. 9. (Color online) Transmission contrast versus measured Q factor of Type I defect modes for $N = 4$ (left) and $N = 6$ (right).

($Q = \lambda/\Delta\lambda$), instead of from curve fitting the transmission spectra. As expected, the Q factor increases as the detuning toward the midgap decreases. The maximum Q factor obtainable from our structure is $\sim 3 \times 10^{-4}$, which suggests enhancement of $\sim$30× relative to the Q factor of the individual resonator. The sensitivity of the Q factor with the detuning is clearly evident in Fig. 8. A change of ~0.1 in the normalized detuning can readily decrease the Q factor by a factor of more than 5. This sensitivity can be reduced by adding more unit cells in the subarrays, as shown in the right panel of Fig. 8, where each subarray size is increased to six unit cells.

As expected, the Q-factor dependence with normalized detuning has decreased, where a change of ~0.1 in normalized detuning decreases the Q factor by a factor of less than 2. This is because the bandgap is better defined in the structure that has more unit cells and corresponds to a much flatter reflection spectrum. However, this does not necessarily mean that the Q factor for resonance near the midgap is higher. In fact, the maximum Q factor for $N = 6$ remains about the same as in the case for $N = 4$, which is $\sim 3 \times 10^4$. Indeed, this is consistent with the previous measurement of $Q_{\text{int}} \sim 6 \times 10^4$ from an individual racetrack resonator, which suggests the maximum obtainable loaded Q factor of $\sim 3 \times 10^4$.

The transmission contrast of defect modes for $N = 4$ and $N = 6$ are plotted against their corresponding Q factors in Fig. 9. The transmission contrast is directly measured as the ratio between the peak transmission and the highest background transmission. Generally, it can be observed that the transmission contrast becomes higher at the increasing Q factor. This is quite different from what is usually the case, where the effect of loss is more pronounced in higher Q and translates to lower transmission contrast. This is because in Type I structures the transmission contrast is affected more by the envelope effect of the background spectrum than by the cavity loss. This can clearly be seen in the low-Q and low contrast defect mode near the band edges (see Fig. 7). Furthermore, it is also apparent that the transmission contrast for $N = 6$ is higher than that of $N = 4$ at high Q values. This again is attributed to a better defined photonic bandgap in more unit cells, which gives results to less envelope effect.

B. Type II Defect Modes

The Type II defect mode structure consists of mutually coupled resonator arrays with an elongated resonator in the center, where the subarrays of $N = 2$ and $N = 3$ unit cells

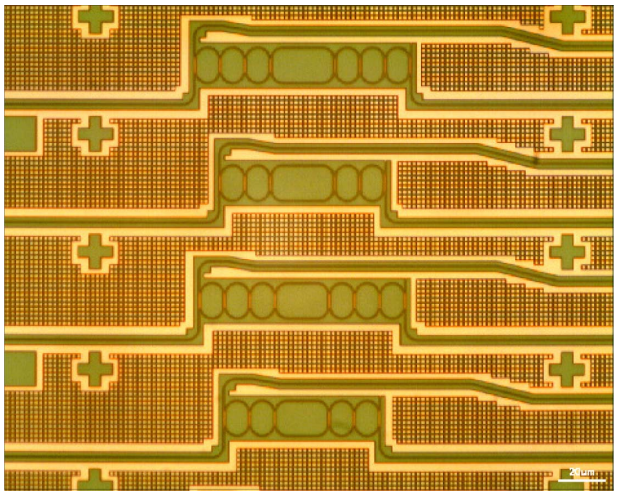

Fig. 10. (Color online) Optical micrographs of the fabricated Type II defect mode structures for $N = 2$ and $N = 3$.

are fabricated for each defect size (see Fig. 10). The cavity length of the regular resonator is $L_{\text{cav}} = 2\pi R + 2L_C$, where L_C is the coupler length and R is the ring radius. The defect ring cavity length, on the other hand, is $L_d = (2\pi R + 2L_C + 2L)$, where L is the elongation parameter. Both the ring radius and the coupler length are fixed to 5 μm, while the elongation parameter L is adjusted from 0 μm to 20.7 μm to realize a defect size from $k_d \sim 1.0$ (identical rings) to $k_d \sim 2.0$. The transmission spectra of Type II defect modes corresponding to different defect sizes are shown in Fig. 11, where the cases for $N = 2$ and $N = 3$ are presented in left and right panels, respectively.

The band structure of Type II structures follows that of CROW, where the photonic bandgap is formed around the antiresonance and depends inversely on the interresonator coupling strengths [17]. This is clearly reflected in Fig. 11 at $k_d \sim 1.0$, when the Type II structure behaves as CROW. The manifestation of the photonic bandgap can be observed in the flat stop band in the transmission spectrum and is denoted within the shaded region. As k_d is increased, we can see that the defect mode moves farther from the band edge toward the midgap, indicating the movement of donorlike

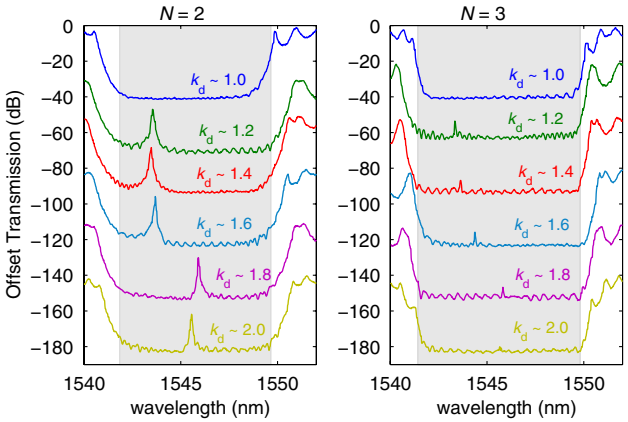

Fig. 11. (Color online) Offset transmission of Type II defect mode structure for different defect sizes and subarray unit cells. The elongation lengths corresponding to each defect size are 0 μm, 4.2 μm, 8.3 μm, 12.4 μm, 16.6 μm, and 20.7 μm, respectively.

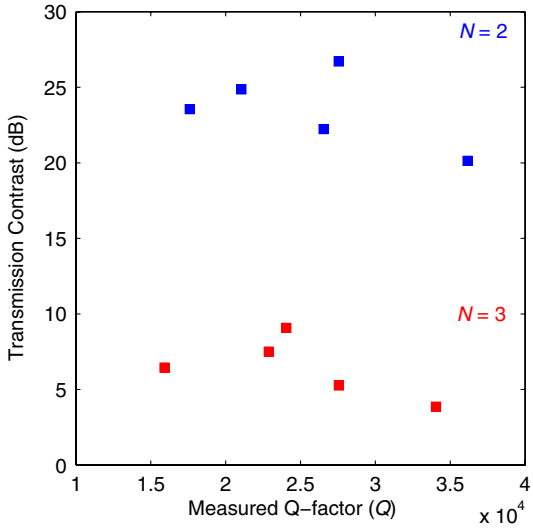

Fig. 12. (Color online) Contrast versus Q factor in Type II defect mode for different units of subarrays. The Q factors are measured in 0.005 nm wavelength resolution.

modes [31]. As expected, the Q factor increases as the defect modes move toward the midgap, with progressively lower transmission contrast.

Although the photonic bandgap is more pronounced for $N = 3$ (see the right panel of Fig. 11), the transmission contrasts are much lower compared to those for $N = 2$ while the Q factor remains relatively unchanged. Figure 12 shows the plot of measured transmission contrasts as a function of measured Q factors for $N = 2$ and $N = 3$. The introduction of one extra unit cell decreases the transmission contrast dramatically by ~20 dB. On the other hand, the Q factor saturates at $\sim 3.5 \times 10^4$ for $N = 3$, which is again to be expected from $Q_{\text{int}} \sim 6 \times 10^4$ of our individual resonators. The maximum Q enhancement obtainable in the Type II structure is ~35×.

It can be seen that the Q factor and transmission contrast for Type II defect modes are inversely dependent on each other, which is the opposite case of those for Type I defect modes. This can be attributed to the complementary photonic bandgap features of both Type I and Type II structures [17]. Since the interaction between resonators intensifies around the resonance for Type I structures, the Type I defect modes interact more with the background spectrum than do Type II defect modes. This gives results in a decreased transmission contrast in the Type I defect mode, especially near the band edge because of the increased background spectrum. For Type II structures, on the other hand, the photonic bandgap occurs around the antiresonance, which means that there is no interresonator interaction when a defect mode is formed. As a result, the transmission contrast is relatively independent from the background spectrum.

4. COMPARISON WITH CRIT STRUCTURE

It is interesting to explore whether there is a relationship between the defect modes demonstrated above and those of EIT-like (or CRIT) in the two-resonator structures. In the CRIT structure, the transparency is realized by coherent interaction of the two resonators having slightly different resonance frequencies. The light is strongly localized within the spacing between the two resonators [5,6], and the Q factor of the

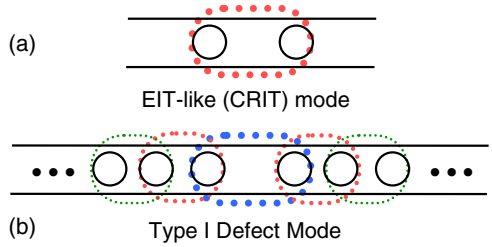

Fig. 13. (Color online) Resemblance between Type I defect mode and EIT-like resonance. The dotted lines denote the field distributions. The line thickness signifies the amplitudes.

transparency is inversely dependent on the resonance frequency detuning between the resonators. Therefore, the Q factor approaches infinity, at least in theory, when the two resonators are exactly identical [9]. On the other hand, in Type I defect modes, the two subarrays provide high reflection and strongly confine the light within the defect. All the resonators are identical and the Q factor is theoretically infinite when the defect resonance is exactly situated at the midgap, as a consequence of unity reflection from the subarrays.

In terms of field distribution, the Type I defect mode bears some degrees of similarity with EIT-like resonance. The case of EIT-like resonance based on a two-resonator structure is illustrated in Fig. 13(a), where the light is strongly localized between two slightly detuned resonators and each of the resonators functions as frequency dependent mirrors [5,9]. On the other hand, the field distribution of the Type I defect mode consists of a cascade of overlapping field distributions that are similar to those in EIT-like resonance, as illustrated in Fig. 13(b). This is also confirmed by FDTD calculation in Fig. 4(a), where the piecewise constant fields along the waveguide are very similar to the field distribution in an EIT-like situation. Thus it can be said that the Type I defect mode is an extension of EIT resonance. Another comparison can be made in terms of amplitude response, where the Type I defect mode becomes increasingly similar to EIT-like resonance as it moves toward the midgap. The rather asymmetric EIT-like spectrum can be seen when $k_d \sim 1.007$, as shown in Fig. 7. Therefore, at the increasing number of resonators, it can be said that EIT-like resonance progressively transforms into the Type I defect mode.

As of Type II defect modes, there is generally spectral similarity between the EIT-resonance and Type II defect modes (see Fig. 11). However, Type II defect modes are not an extension of EIT-like resonance in any way. The EIT-like resonance is heavily dependent on the background spectrum (of the two resonators), while Type II defect mode is almost independent of the background spectrum (see Fig. 12). This is because the coherent interaction between resonators, which is a prerequisite for EIT-like resonance, does not exist in Type II structures when the defect modes are formed within the photonic bandgap.

5. CONCLUSIONS

The study of defect modes in two types of coupled resonator configurations has been presented in this paper. The first type (Type I) is a periodic array of side-coupled identical resonators with two common waveguide buses, while the second type (Type II) is a periodic array of mutually coupled resonators with the first and last resonators side coupled to waveguide buses. The defect is introduced in the form of interstitials (for Type I) and different ring sizes (for Type II). By adopting simple Fabry–Perot analogy and using transfer matrix formalism, the defect modes for both types can be readily mapped as a function of normalized defect sizes. From FDTD calculations, the field distributions corresponding to defect modes have been obtained, where the field amplitude is piecewise constant within the unit cell and decays as it moves away from the defect. The numerically demonstrated field distributions for Type I and Type II defect modes are in excellent agreement with the eigenvectors derived from transfer matrix formalism.

The Type I and Type II defect mode structures are fabricated by the CMOS-compatible 193 nm deep ultraviolet lithography process in silicon-on-insulator technology. The measurement of the Q factor shows that the Q progressively increases as the defect mode moves toward the midgap, with Q enhancement up to ~30× (for Type I) and ~35× (for Type II) relative to the individual resonator. The maximum obtainable Q factor is in the range of $\sim 3 \times 10^4$, in agreement with $\sim 6 \times 10^4$ intrinsic Qfactor measured from the basic resonator structure. The limitation of intrinsic Q has been shown to be caused by resonator geometry, which imparts more loss in the coupling region, limiting the round-trip loss factor up to $a \sim 0.994$ (instead of $a \sim 0.998$ when such coupling loss is absent).

The transmission contrasts of each defect mode are characterized and plotted as a function of measured Q factor for both Type I and Type II defect modes. It is interesting to note that the relationship between transmission contrast and Q factor for Type I defect modes is exactly the opposite of that of the Type II counterparts, which is caused by the complementary photonic bandgap property inherent in both types. Comparison between the coupled resonator–based defect modes and EIT-like resonance is also drawn, which suggests that the Type I defect mode is actually an extension of EIT-like resonance. Such a resemblance, however, is not found in the Type II defect mode.

APPENDIX A: TRANSFER MATRIX FORMALISM FOR TYPE I AND TYPE II MICRORESONATOR ARRAYS

The light propagation in resonator arrays resembles that in layered media in many aspects. In the Type I structure the light resonantly tunnels from one waveguide to another, which makes it functionally identical to a frequency dependent mirror. The interresonator distance, on the other hand, is analogous to the dielectric layer thickness in the multilayered media. In the Type II structure, the cross-coupling and self-coupling coefficients between resonators are analogous to transmittance and reflectance at the interface between two dielectric media. Meanwhile, half of the circumference of each resonator is analogous to individual dielectric layer thicknesses of the multilayered media. Therefore, with the preceding resemblances, it is quite expected to see many similarities between our transfer matrix formalisms and those of layered media [38].

The unit cell of the Type I structure consists of a single resonator side coupled with two parallel bus waveguides, as shown in Fig. 14(a). The transmission (T) and reflection (R) of each unit cell, as denoted by the drop and through transmittances of a single ring resonator, can be expressed as

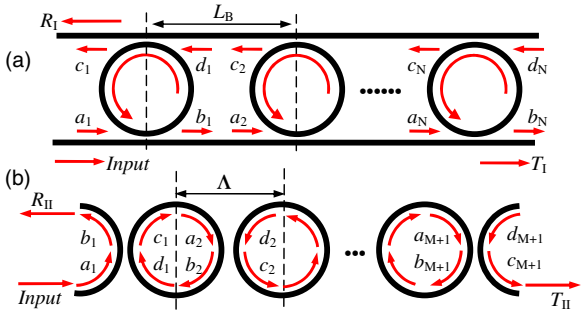

Fig. 14. (Color online) (a) Type I and (b) Type II coupled resonator structures.

$$T = \frac{r - ar\,\exp(-i\delta)}{1 - ar^2\,\exp(-i\delta)},$$
$$R = \frac{-(1-r^2)\exp(-i\delta/2)}{1 - ar^2\,\exp(-i\delta)}, \tag{A1}$$

where a is the round-trip cavity loss, r is the self-coupling coefficient between ring resonator and waveguide, and $\delta = k_0 n_{\text{eff}} L_{\text{cav}}$ is the cavity round-trip phase. The field amplitudes in the left $[c \quad a]^T$ and right $[d \quad b]^T$ planes of the unit cell can be formulated in the following matrix:

$$\begin{bmatrix} d \\ b \end{bmatrix} = \frac{1}{T}\begin{bmatrix} 1 & -R \\ R & T^2 - R^2 \end{bmatrix}\begin{bmatrix} c \\ a \end{bmatrix}, \tag{A2}$$

where in the lossless case several corollaries can be derived: (i) $|R + T| = 1$; (ii) R/T is pure imaginary; and (iii) $(T^2 - R^2)/T = 1/T*$, which are useful in simplifying the characteristic equation for band calculation [17]. The unit cells are separated by L_B, which introduces propagator matrix

$$\begin{bmatrix} d \\ b \end{bmatrix}_n = \begin{bmatrix} \exp(-i\delta_B) & 0 \\ 0 & \exp(i\delta_B) \end{bmatrix}\begin{bmatrix} c \\ a \end{bmatrix}_{n+1}. \tag{A3}$$

The interresonator distance L_B is assumed to be sufficiently large such that the direct coupling between resonators is negligible. Thus, the transfer matrix in lossless case can be described as

$$\begin{aligned}\begin{bmatrix} c \\ a \end{bmatrix}_{n+1} &\equiv \begin{bmatrix} m_{11} & m_{12} \\ m_{21} & m_{22} \end{bmatrix}\begin{bmatrix} c \\ a \end{bmatrix}_n \\ &= \begin{bmatrix} \frac{1}{T}\exp(i\delta_B) & -\frac{R}{T}\exp(i\delta_B) \\ \frac{R}{T}\exp(-i\delta_B) & \frac{1}{T*}\exp(-i\delta_B) \end{bmatrix}\begin{bmatrix} c \\ a \end{bmatrix}_n.\end{aligned} \tag{A4}$$

The unit cell for the Type II structure is a single resonator mutually coupled to its neighboring resonators, as shown in Fig. 14(b). By relating the field amplitudes inside the resonator, $a_{n+1} = c_n \exp(-i\delta/2)$, $d_n = b_{n+1}\exp(-i\delta/2)$, the transfer matrix can be written as

$$\begin{aligned}\begin{bmatrix} a \\ b \end{bmatrix}_{n+1} &\equiv \begin{bmatrix} p_{11} & p_{12} \\ p_{21} & p_{22} \end{bmatrix}\begin{bmatrix} a \\ b \end{bmatrix}_n \\ &= \frac{1}{i\sqrt{1-r^2}}\begin{bmatrix} -\exp\left(-i\frac{\delta}{2}\right) & r\exp\left(-i\frac{\delta}{2}\right) \\ -r\exp\left(i\frac{\delta}{2}\right) & \exp\left(i\frac{\delta}{2}\right) \end{bmatrix}\begin{bmatrix} a \\ b \end{bmatrix}_n.\end{aligned} \tag{A5}$$

ACKNOWLEDGMENTS

The authors thank Pieter Dumon for the device fabrication under ePIXnet platform. This work was supported by the National Research Foundation, Singapore, under NRF-G-CRP 2007-01, by the Ministry of Education (MOE), Singapore, under ARC 16/07, and by the Asian Office of Aerospace Research (AOARD).

REFERENCES

1. J. B. Khurgin, "Optical buffers based on slow light in electromagnetically induced transparent media and coupled resonator structures: comparative analysis," J. Opt. Soc. Am. B **22**, 1062–1074 (2005).
2. S. E. Harris, "Electromagnetically induced transparency," Phys. Today **50**, 36–42 (1997).
3. L. V. Hau, S. E. Harris, Z. Dutton, and C. H. Behroozi, "Light speed reduction to 17 metres per second in an ultracold atomic gas," Nature **397**, 594–598 (1999).
4. M. F. Yanik and S. Fan, "Stopping and storing light coherently," Phys. Rev. A **71**, 013803 (2005).
5. Q. Xu, S. Sandhu, M. L. Povinelli, J. Shakya, S. Fan, and M. Lipson, "Experimental realization of an on-chip all-optical analogue to electromagnetically induced transparency," Phys. Rev. Lett. **96**, 123901 (2006).
6. X. Yang, M. Yu, D.-L. Kwong, and C. W. Wong, "All-optical analog to electromagnetically induced transparency in multiple coupled photonic crystal cavities," Phys. Rev. Lett. **102**, 173902 (2009).
7. D. D. Smith, H. Chang, K. A. Fuller, A. T. Rosenberger, and R. W. Boyd, "Coupled-resonator-induced transparency," Phys. Rev. A **69**, 063804 (2004).
8. N. G. Farca, S. I. Shopova, and A. T. Rosenberger, "Induced transparency and absorption in coupled whispering-gallery microresonators," Phys. Rev. A **71**, 043804 (2005).
9. L. B. Maleki, A. B. Matsko, A. A. Savchenkov, and V. S. Ilchenko, "Tunable delay line with interacting whispering-gallery-mode resonator," Opt. Lett. **29**, 626–628 (2004).
10. L. Y. Mario, D. C. S. Lim, and M. K. Chin, "Proposal of an ultranarrow passband using two-coupled rings," IEEE Photon. Technol. Lett. **19**, 1688–1690 (2007).
11. L. Y. M. Tobing, P. Dumon, R. Baets, D. C. S. Lim, and M. K. Chin, "Finesse enhancement in silicon-on-insulator two-ring resonator system," Appl. Phys. Lett. **92**, 101122 (2008).
12. B. Maes, P. Bienstman, and R. Baets, "Switching in coupled nonlinear photonic crystal resonators," J. Opt. Soc. Am. B **22** (8), 1778–1784 (2005).
13. Y. Lu, J. Yao, X. Li, and P. Wang, "Tunable asymmetrical Fano resonance and bistability in microcavity-resonator Mach Zehnder interferometer," Opt. Lett. **30**, 3069–3071 (2005).
14. J. E. Heebner, P. Chak, S. Pereira, J. E. Sipe, and R. W. Boyd, "Distributed and localized feedback in microresonator sequence for linear and nonlinear optics," J. Opt. Soc. Am. B **21**, 1818–1832 (2004).
15. Z. Wang and S. Fan, "Compact all-pass filters in photonic crystals as the building block for high-capacity optical delay lines," Phys. Rev. E **68**, 066616 (2003).
16. A. Yariv, Y. Xu, R. K. Lee, and A. Scherer, "Coupled-resonator optical waveguide: a proposal and analysis," Opt. Lett. **24**, 711–713 (1999).
17. Y. M. Landobasa, S. Darmawan, and M. K. Chin, "Matrix analysis of 2-D micro-resonator lattice optical filters," IEEE J. Quantum Electron. **41**, 1410–1418 (2005).
18. F. Xia, L. Sekaric, and Y. Vlasov, "Ultracompact optical buffers on a silicon chip," Nature **1**, 65–71 (2007).
19. J. K. S. Poon, J. Scheuer, Y. Xu, and A. Yariv, "Designing coupled-resonator optical delay lines," J. Opt. Soc. B **21**, 1665–1673 (2004).
20. L. Y. M. Tobing, P. Dumon, R. Baets, and M. K. Chin, "Boxlike filter response based on complementary photonic bandgap in two-dimensional microresonator arrays," Opt. Lett. **33**, 2512–2514 (2008).

21. S. Xiao, M. H. Khan, H. Shen, and M. Qi, "Silicon-on-insulator microring add-drop filters with free spectral ranges over 30 nm," J. Lightwave Technol. **26**, 228–236 (2008).
22. T. Barwicz, M. Popovic, M. R. Watts, P. T. Rakich, E. P. Ippen, and H. I. Smith, "Fabrication of add-drop filters based on frequency-matched microring resonators," J. Lightwave Technol. **24**, 2207–2218 (2006).
23. F. Xia, M. Rooks, L. Sekaric, and Y. Vlassov, "Ultra-compact high order ring resonator filters using submicron silicon photonic wires for on-chip optical interconnects," Opt. Express **15**, 11934–11941 (2007).
24. J. R. Ong, M. L. Cooper, G. Gupta, W. M. Green, S. Assefa, F. Xia, Y. A. Vlasov, and S. Mookherjea, "Intra- and inter-band four-wave mixing in silicon coupled resonator optical waveguides," in *CLEO:2011–Laser Applications to Photonic Applications*, OSA Technical Digest (CD) (Optical Society of America, 2011), paper CTuW1.
25. I. Chremmos and O. Schwelb, "Diatomic coupled-resonator optical waveguide," J. Opt. Soc. B **27**, 1242–1251 (2010).
26. O. Schwelb and I. Frigyes, "All-optical tunable filters built with discontinuity-assisted ring resonators," J. Lightwave Technol. **19**, 380–386 (2001).
27. X. Tu, L. Y. Mario, and T. Mei, "Coupled Fano resonator," Opt. Express **18**, 18820–18831 (2010).
28. E. Yablonovitch, "Inhibited spontaneous emission in solid-state physics and electronics," Phys. Rev. Lett. **58**, 2059–2062 (1987).
29. Y. M. Landobasa and M. K. Chin, "Defect modes in micro-ring resonator arrays," Opt. Express **13**, 7800–7815 (2005).
30. O. Schwelb and I. Chremmos, "Defect assisted coupled resonator optical waveguide: weak perturbations," Opt. Commun. **283**, 3686–3690 (2010).
31. L. Y. M. Tobing, P. Dumon, R. Baets, and M. K. Chin, "Demonstration of defect modes in coupled microresonator arrays fabricated in silicon-on-insulator technology," Opt. Lett. **33**, 1939–1941 (2008).
32. www.epixfab.eu.
33. L. Y. Mario, D. C. S. Lim, P. Dumon, R. Baets, and M.-K. Chin, "Experimental verification of finesse enhancement scheme in two-ring resonator system," Proc. SPIE **6996**, 69960B (2008).
34. A. Yariv, "Critical coupling and its control in optical waveguide-ring resonator systems," IEEE Photon. Technol. Lett. **14**, 483–485 (2002).
35. F. Xia, L. Sekaric, and Y. A. Vlasov, "Mode conversion losses in silicon-on-insulator photonic wire based racetrack resonators," Opt. Express **14**, 3872–3886 (2006).
36. V. Van, P. P. Absil, J. V. Hryniewicz, and P.-T. Ho, "Propagation loss in single-mode GaAs-AlGaAs microring resonators: measurement and model," J. Lightwave Technol. **19**, 1734–1739 (2001).
37. M. Mancinelli, R. Guider, M. Masi, P. Bettotti, M. R. Vanacharla, J.-M. Fedelli, and L. Pavesi, "Optical characterization of a SCISSOR device," Opt. Express **19**, 13664–13674 (2011).
38. P. Yeh, *Optical Waves in Layered Media* (Wiley, 2005).